Morphing Blades for Tidal Turbines: a Theoretical Study

Citation for published version:
Pisetta, G, Le Mestre, R & Viola, IM 2022, 'Morphing Blades for Tidal Turbines: a Theoretical Study', *Renewable Energy*, vol. 183, pp. 802-819. https://doi.org/10.1016/j.renene.2021.10.085

Digital Object Identifier (DOI):
10.1016/j.renene.2021.10.085

Link:
Link to publication record in Edinburgh Research Explorer

Document Version:
Peer reviewed version

Published In:
Renewable Energy

Morphing Blades for Tidal Turbines: a Theoretical Study

Gabriele Pisetta[a], Robin Le Mestre[a,b], Ignazio Maria Viola[a,]

[a]School of Engineering, Institute for Energy Systems, University of Edinburgh, Edinburgh, United Kingdom
[b]École Normale Supérieure Paris-Saclay, Cachan, France

Abstract

Tidal energy has the potential to significantly contribute to energy security by providing predictable renewable energy. New technology is needed to decrease the levelised cost of energy and to make this energy sector competitive in the energy market. A key area where technology can contribute to decrease costs is mitigating the hydrodynamic load fluctuations, and thus increasing the fatigue life of the turbine. Here, we formulate a passive morphing blade concept that aims to mitigate the unsteady thrust without affecting the mean torque and thus the harvested power.

We show that a blade with a trailing edge that deflects perfectly elastically can suppress virtually all fluctuations without varying the mean loads. The effect of the hydrodynamic and blade's inertia, the material damping, and the radial shear stress, decrease the performances.

Using a low-order model of the blade, we show that when a gust occurs, the angle of attack experienced by a rigid blade increases, whilst that experienced by a well-designed morphing blade decreases. This counter-intuitive mechanism is what makes morphing blades highly effective. While blades that could passively twist have previously been developed, this theoretical study suggests that chordwise flexibility is a suitable alternative that should be further explored.

Keywords: unsteady load mitigation, passive load control, pitch control, morphing, fluid-structure interaction, tidal turbine

Nomenclature

A area swept by the blade [m^2]

A^{2D} perimeter of a blade annulus [m]

$C(k)$ Theodorsen's function [-]

C^{c}_{am} circulatory damping coefficient [Nm $s^{-1}deg^{-1}$]

C^{nc}_{am} non-circulatory damping coefficient [Nm $s^{-1}deg^{-1}$]

C_κ stiffness coefficient [-]

C^{dy}_κ optimal stiffness coefficient (dynamic analysis) [-]

C^{qs}_κ optimal stiffness coefficient (quasi-steady analysis) [-]

C_{RBM} root bending moment coefficient [-]

C_{tot} total damping [Nm $s^{-1}deg^{-1}$]

C_μ damping coefficient [-]

C_D drag coefficient [-]

C_L lift coefficient [-]

C_M foil's pitching moment coefficient [Nm]

C_P power coefficient [-]

C_P^{2D} sectional power coefficient [-]

C_T thrust coefficient [-]

C_T^{2D} sectional thrust coefficient [-]

D drag force [N]

F force [N]

F_{Co} Coriolis force [N]

F_{Eu} Euler force [N]

F_{c} centrifugal force [N]

I_{am} added mass coefficient [Nm s^2deg^{-1}]

J blade pitching inertia [kgm^2]

J^{2D} blade section inertia [kgm]

J_{tot} total inertia [kgm^2]

K_{am} added stiffness coefficient [$Nmdeg^{-1}$]

K_{tot} total stiffness [$Nmdeg^{-1}$]

L lift force [N]

M pitching moment [Nm]

M_{c}^{2D} sectional centrifugal moment [N]

M_{dy}^{2D} hydrodynamic moment on a blade section [N]

M_{qs}^{2D} sectional quasi-steady hydrostatic moment [N]

M_{RB} root bending moment [Nm]

M_{c} blade centrifugal moment [Nm]

M_{dy} hydrodynamic moment on the blade [Nm]

M_{qs} blade quasi-steady hydrostatic moment [Nm]

M_{s} spring moment [Nm]

$M_{\mathrm{s}}^{2\mathrm{D}}$ spring moment per unit span [N]

N number of blade sections [-]

N_b number of blades [-]

P blade power [W]

P power extracted [W]

$P^{2\mathrm{D}}$ sectional power [Wm^{-1}]

R tip radius [m]

T blade thrust force [N]

T thrust force [N]

$T^{2\mathrm{D}}$ sectional thrust force [Nm^{-1}]

U inflow velocity [m s^{-1}]

U_{hub} free stream velocity at hub height [m s^{-1}]

U_x axial component of the inflow velocity [m s^{-1}]

U_∞ free stream velocity [m s^{-1}]

U_ψ tangential component of the inflow velocity [m s^{-1}]

ZZ' plane of a generic blade section [-]

$\boldsymbol{A}$ position of the pitching axis of a section [m]

$\boldsymbol{B}$ position of a generic point on a section [m]

$\overline{\boldsymbol{AB}}$ distance of a generic point from the pitching axis of a section [m]

δr span of a section [m]

γ angular coordinate on a blade section [m]

$\hat{C}_M$ flat plate's pitching moment coefficient [Nm]

$\hat{F}$ Prandtl's tip loss factor [-]

$\hat{J}$ objective function of the optimisation problem [-]

$\hat{x}$ chordwise coordinate on a blade section [m]

$\hat{x}_A$ distance of the pitching axis from the leading edge of a section [m]

Re Reynolds number [-]

μ blade mechanical damping [Nm s^{-1}deg^{-1}]

ψ	blade azimuthal position [deg]
a	axial induction factor [-]
a'	tangential induction factor [-]
b	half-chord length [m]
c	chord length [m]
d	distance of the pitching axis from the half chord [m]
f	Prandtl's tip loss factor exponent [-]
m	mass of a small blade element [kg]
r	radial coordinate [m]
t	time [s]
x	horizontal streamwise coordinate [m]
xy	foil thickness in percentage of chord [-]
z	vertical coordinate from the seabed [m]
z_{hub}	height of the hub from the seabed [m]
Γ	sectional non-dimensional stiffness [-]
Γ_0	optimal sectional non-dimensional stiffness [-]
Ω_N	system natural frequency [radss^{-1}]
Ω_{s}	blade cross-sectional shell area [m^2]
Ω_{w}	blade cross-sectional internal area [m^2]
α	angle of attack [deg]
β	pitch angle [deg]
β_0	twist angle [deg]
κ	stiffness of the spring [Nmdeg^{-1}]
κ^{2D}	spring stiffness per unit span [Ndeg^{-1}]
λ	tip speed ratio [-]
λ_0	optimal tip speed ratio [-]
ω	rotational speed [rads^{-1}]
ϕ	inflow angle [deg]
ρ_{s}	density of blade shell [kgm^{-3}]
ρ_{w}	density of water [kgm^{-3}]
θ	spring strain angle [deg]
θ^{dy}	spring strain angle (dynamic analysis) [deg]
θ_0^{dy}	optimal preload (dynamic analysis) [deg]
θ^{qs}	spring strain angle (quasi-steady analysis) [deg]

θ_0^{qs} optimal preload (quasi-steady analysis) [deg]

θ_0 preload of the spring [deg]

ζ damping ratio [-]

BEMT Blade Element Momentum Theory

HATT Horizontal Axis Tidal Turbine

HAWT Horizontal Axis Wind Turbine

LCOE Levelised Cost Of Energy

TGL Tidal Generation Limited

Nomenclature note: time derivatives are shown with a dot above the variable; overbars show mean values over a blade revolution; bold symbols describe vector variables; Δ represents the difference between the maximum and minimum values of a fluctuating variable; δ represents a small variation; quantities that refer to the rigid fixed-pitch turbine are indicated by subscripts $|_{\kappa\to\infty}$.

1. Introduction

Tidal energy is a promising renewable energy source that could critically contribute to energy security [1]. It's been estimated that the global theoretical potential of tidal power is 22000 TWh/year, and that under favourable conditions, by 2050, wave and tidal energy systems could contribute to nearly 10% of the European electrical demand (350 TWh/year) [2]. The world's first arrays of tidal turbines (Meygen and Nova's Bluemull Sound, 2016) have only recently been deployed in Scotland. For this energy sector to develop further, new technology must be developed to reduce the levelised cost of energy (LCOE), which is the minimum constant price at which electricity has to be sold in order to break-even over the lifetime of the project. Technology that enables more reliable and cheaper tidal turbines to be built would contribute to a reduction in the LCOE and it would provide more competitive renewable energy.

The large load fluctuations induced by the shear and turbulence of the onset flow, wave-induced current fluctuations, yaw misalignment, interaction with the support structures, and wakes of the upstream devices present a major challenge to the design of tidal turbines [3, 4]. Load fluctuations are transmitted from the blades to the rest of the turbine making fatigue failures a key limit to reliability [5]. To increase local blockage and thus yields, tidal turbines might be placed in close proximity. This will have consequences on, for example, the foundations and scours [6, 7, 8], but will also result in additional unsteady load fluctuations [9]. Furthermore, unsteady loads are reflected in power output fluctuations, which result in over-dimensioned power-take-off systems [10] and in a lower maximum mean operating power. Therefore, unsteady load mitigation is critical to reducing LCOE and enhancing the competitiveness of tidal energy.

Load fluctuations are currently mitigated by actively varying the turbine speed, by actively pitching the blades, or by enabling the blade to twist passively to feather when the fluid dynamic load increases (also known as hydroelastic tailoring) [11]. Unfortunately, the effectiveness of these control systems decreases with the size of the blade. In fact, there is a trade off between the power that can be spent to actively control the rotor and the highest frequency that can be mitigated. From the results of Barlas *et al.* [12, 13], for example, it can be noted that pitch control is up to about 50 times slower than required to cancel up to the highest load fluctuations experienced by wind turbines. Passive twist is currently adopted by Schottel Hydro, whose 70 kW turbines are 6.3 m in diameter. On the other hand, the higher loads on SIMEC Atlantis Energy's MW-scale tidal turbines are incompatible with the flexibility required for passive twist. Additionally, all these mechanisms primarily mitigate the unsteady load at the tip, which is the major contribution to the torque and thrust, but they do not prevent large flow separation from occurring near the blade root [3]. This results in less energy remaining available to the downstream turbines, and thus to lower efficiency for compacted arrays.

Fast-actuated flaps, like those used on aircraft wings, could mitigate higher frequency fluctuations [12, 13, 14]. These flaps are smaller and therefore could have a faster response than a whole blade pitching system, but they still require power electronics, hinges with bearings and actuator mechanisms that are exposed to debris and biofouling. This additional complexity of the system is seen by industry as posing a risk to turbine reliability. The cost of maintenance of both offshore wind and tidal turbines is a major driver compared to onshore wind. Hence, reliability is paramount [15]. For example, tidal companies such as Nova Innovation, Nautricity and Schottel Hydro adopt fixed blade turbines to maximise reliability. Orbital Marine Power and SIMEC Atlantis Energy, which operate the largest rotors, only use collective pitch control, which cannot mitigate fast load fluctuations due to, for example, shear, interference, yaw misalignment, etc.

Last year, the European Commission identified blades with built-in chordwise flexibility as one of the most promising concepts for reducing the costs of the blades and the downstream components of turbines [16]. Hence, in this paper we investigate the underlying principles of load alleviation through morphing blades and their potential effectiveness.

Specifically, we aim to answer the following research questions. (1) How do morphing blades work? What are the physical phenomena that underlie unsteady load alleviation by morphing blades? (2) Which are the key factors of a practical implementation that can decrease their effectiveness? To address these questions, we develop a low-order model of a morphing blade and we identify the parameters that govern the system performance.

This work focuses on the underlying physical mechanism and aims to pave the way to future designs. The proposed model is kept as simple as possible to allow insights on the physics, whilst it does not mean to be a design tool. While the model cannot be currently validated due to the lack of experimental data on morphing blades, we test our model of rigid and flexible blades against the numerical simulations of other authors. We consider both the unsteady fluctuations due to the rotation of the blades in a steady shear current, and those due to a turbulent shear current in the presence of large waves. The latter input flow velocity condition is taken from full-scale measurements undertaken at the European Marine Energy Centre (EMEC) tidal test site [3].

The rest of the paper is organised as follows. In Section 2, we present our methodology and how we modelled the morphing blade. In Sections 4, 5 we present the model inputs and the turbine geometry, and the model validation respectively. Section 6 shows the analysis of the morphing blade model, how we optimised its load alleviation capabilities, we present a parametric study of the effect of the morphing blade properties on the system performance, and we show the potential load mitigation of morphing blades on a turbine subjected to real flow conditions. In Section 7, we summarise our findings.

2. Methodology

We present our methodology for a turbine subjected to flow fluctuations caused by a modelled shear flow. Nonetheless, the method can be readily generalised for flow fluctuations induced by other sources, like turbulence, waves and wakes, or for real flow conditions, as described in Section 3. The specific flow conditions, the turbine properties, and the spatial and temporal discretizations are introduced in Section 4.

2.1. Rigid Blade Model

We consider a 3 blades tidal turbine with a rotor diameter of 18 m (blade length $R = 9$ m) operating in a sheared velocity profile, at the optimal tip speed ratio of 4.5. The turbine hub is at 20 m from the seabed, the mean flow velocity at the hub is $U_{\mathrm{hub}} = 2$ m s^{-1}, and the velocity profile varies with a 1/7 power law. Each blade experiences periodic onset flow, such that the inflow speed and the angle of attack are maximum for each section when the blade is pointing upwards, and minimum when pointing downwards. The 1/7 power law is commonly used to describe the velocity profile across a turbulent boundary layer [17]. It is often applied to tidal flow in coastal regions [18], and its use is recommended by the UK Health and Safety Executive [19] to model velocity profiles in coastal regions around the UK.

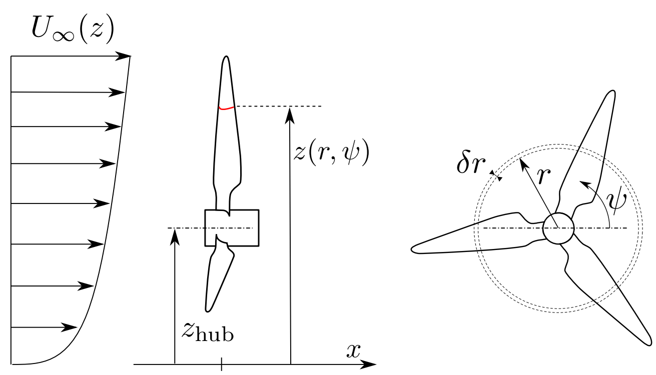

Figure 1: Schematic diagram of a tidal turbine coordinate systems. On the left, the side view shows the interaction of the turbine with a shear flow. On the right, front view of the turbine.

We employ Blade Element Momentum Theory (BEMT) [20] to compute the axial induction factor a and the tangential induction factor a'. The axial (U_x) and tangential (U_ψ) components of the flow speed relative to the blade sections are depicted in Fig. 2 and they are computed following the approach of Burton et al. [20] as

$$
\begin{aligned}
U_x &= U_\infty - a\overline{U}_\infty, \\
U_\psi &= \omega r(1 + a'),
\end{aligned}
\tag{1}
$$

where ω is the turbine rotational speed, r is the section position along the blade, and $\overline{U}_\infty$ is the average upstream axial velocity seen by a blade rotating in a shear flow.

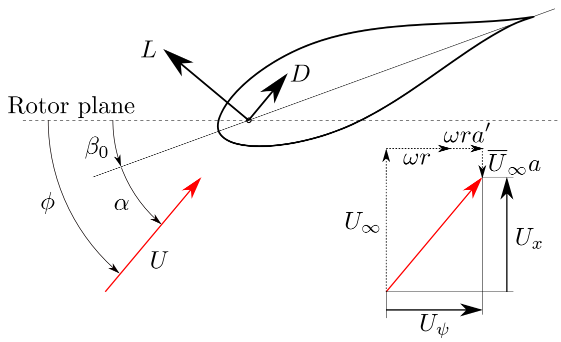

Figure 2: Flow velocities and forces acting on a 2D blade section.

From the vectors shown in Fig. 2, the flow relative to the blade is obtained as

$$
\begin{aligned}
U &= \sqrt{U_x^2 + U_\psi^2}, \\
\phi &= \tan^{-1}\left(\frac{U_x}{U_\psi}\right),
\end{aligned}
\tag{2}
$$

where U is the magnitude of the relative flow speed experienced by the blade section and ϕ is the inflow angle (Fig. 2). Let β_0 be the twist angle of a blade section, the angle of attack is

$$
\alpha = \phi - \beta_0. \tag{3}
$$

We compute the tip loss factor following Burton et al. [20] as

$$
\hat{F} = \frac{2}{\pi}\cos^{-1}(e^{-f}), \tag{4}
$$

where

$$f = \frac{N_b}{2}\frac{1-r}{r\sin\phi}, \tag{5}$$

and N_b is the number of blades.

The BEMT algorithm evaluates the induction factors with an iterative procedure that uses the mean loads acting on each section. We define the mean inflow conditions as

$$\begin{aligned} \overline{U} &= \sqrt{\overline{U}_x^2 + U_\psi^2}, \\ \overline{\phi} &= \operatorname{atan}\left(\frac{\overline{U}_x}{U_\psi}\right), \end{aligned} \tag{6}$$

where $\overline{U}_x = \overline{U}_\infty(1-a)$. The average angle of attack experienced by each section is

$$\overline{\alpha} = \overline{\phi} - \beta_0. \tag{7}$$

The mean lift and drag coefficients, $C_L(\overline{\alpha})$ and $C_D(\overline{\alpha})$ respectively, are initially evaluated with $a = {}^1/_3$ and $a' = 0$ for each section. The resulting lift and drag are then used to update the values of the induction factors

$$\begin{aligned} a &= \left(\frac{4\pi r\hat{F}\sin\overline{\phi}^2}{N_b c(C_L\cos\overline{\phi} + C_D\sin\overline{\phi})} + 1\right)^{-1}, \\ a' &= \left(\frac{4\pi r\hat{F}\sin\overline{\phi}\cos\overline{\phi}}{N_b c(C_L\sin\overline{\phi} - C_D\cos\overline{\phi})} - 1\right)^{-1}, \end{aligned} \tag{8}$$

where c is the foil's chord.

The procedure is repeated until a, a', C_L and C_D converge.

The performance of the turbine is evaluated in terms of the non-dimensional power and thrust coefficients. For a blade section, they are respectively defined as

$$
\begin{aligned}
C_P^{\mathrm{2D}} &= \frac{P^{\mathrm{2D}}}{\frac{1}{2}\rho_w U_{\mathrm{hub}}^3 A^{\mathrm{2D}}}, \\
C_T^{\mathrm{2D}} &= \frac{T^{\mathrm{2D}}}{\frac{1}{2}\rho_w U_{\mathrm{hub}}^2 A^{\mathrm{2D}}},
\end{aligned}
\tag{9}
$$

where ρ_w is the water density, $A^{\mathrm{2D}} = 2\pi r$ is the perimeter swept by the blade section at spanwise position r, and the thrust T^{2D} and the power P^{2D} are

$$
\begin{aligned}
T^{\mathrm{2D}} &= L\cos\phi + D\sin\phi, \\
P^{\mathrm{2D}} &= \omega r\big(L\sin\phi - D\cos\phi\big).
\end{aligned}
\tag{10}
$$

For a turbine's blade, these coefficients are computed respectively as

$$
\begin{aligned}
C_P &= \frac{P}{\frac{1}{2}\rho_w U_{\mathrm{hub}}^3 A}, \\
C_T &= \frac{T}{\frac{1}{2}\rho_w U_{\mathrm{hub}}^2 A},
\end{aligned}
\tag{11}
$$

where $A = \pi R^2$ is the area swept by the turbine, $T = \sum_i T_i^{\mathrm{2D}} \delta r_i$ and $P = \sum_i P_i^{\mathrm{2D}} \delta r_i$, for $i = 1...N$, where δr_i is the thickness of the section and is chosen sufficiently small to ensure the desired accuracy.

2.2. Morphing Blade Model

The blade can bend its trailing edge to mitigate the changes in the flow incidence, thus alleviating the load fluctuations. Let's assume that the loads on a blade section result in the elastic deformation of the foil as shown in Fig. 3. We consider the effect of such geometric variation as an equivalent change in the angle of attack of the original foil. Therefore, the shape deformation is analogous to the pitch rotation of a rigid foil, and its flexibility can be modelled by a torsional spring with constant properties that controls the pitching motion of the blade (Fig. 4). The angular position of the blade is thus determined by the balance of the moments acting along the pitch axis.

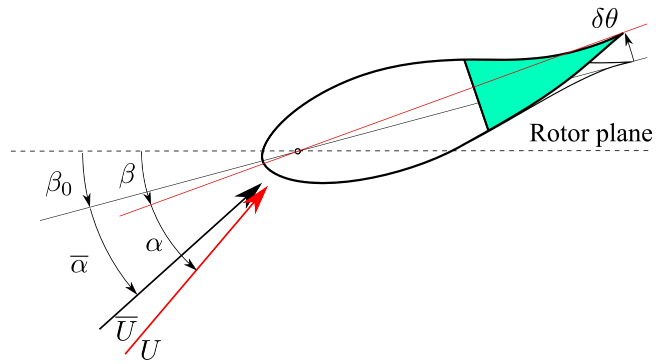

Figure 3: Morphing blade concept. Part of the blade can bend to mitigate inflow fluctuations.

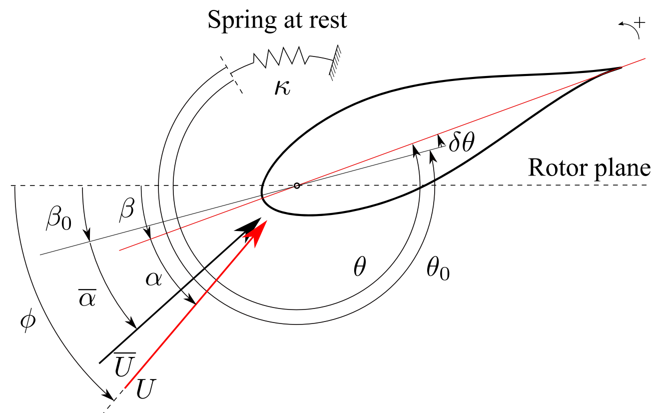

Figure 4: Morphing blade model. The flexibility is modelled by a torsional spring.

The analysis is carried out for two different scenarios. Firstly, we consider a blade where there is no interaction between the sections such that each section moves independently from the others (Fig. 5a). This condition is representative, for example, of a blade made of a flexible material with a very low shear modulus, such that the shear stresses between the sections are negligible. The blade flexibility is represented by a torsional spring for each section, and the deflection of each section is determined by the local flow conditions. This model is described using a 2-dimensional analysis in Section 2.3, and it is optimised for each section of the blade, to allow the same mean load as the rigid foil and to minimise the fluctuations.

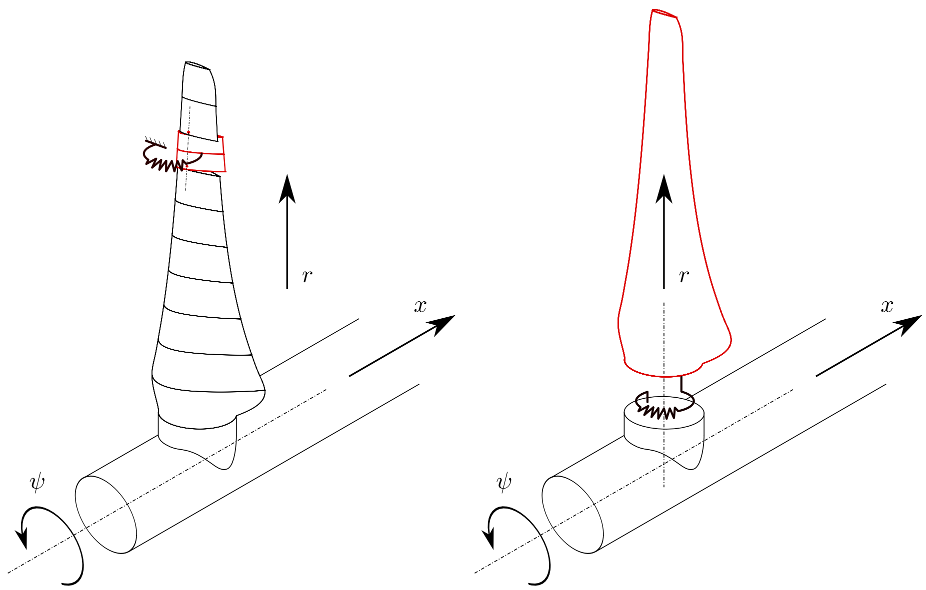

(a) Each section moves independently.

(b) All the sections deflect together.

Figure 5: Morphing blade models.

Secondly, we consider a blade where all sections experience the same deflection along the span (Fig. 5b). As opposed to the previous scenario, this model could represent a blade material with a very high shear modulus. Therefore, the stresses caused by the external loads are efficiently redistributed along the blade such that each section deforms by the same amount. The blade deflection is thus seen as a rigid rotation with the flexibility concentrated at the root of the blade. This flexible connection is modelled with a torsional spring placed at the root that adds a variable pitch angle $\delta\theta$ to the rigid blade twist angle β_0. This condition is presented in Section 2.4, where the entire blade is considered, and the spring's parameters are optimised to minimise the fluctuations in the root bending moment without reducing the average power extracted. In Section 2.5, we extend such model to include the dynamics of the blade and the unsteadiness of the flow, to check the robustness of the optimal system when the blade dynamics are considered, and to investigate the effect of the blade inertia, the unsteady hydrodynamics and the blade mechanical damping on the performance of the morphing blade.

2.3. Quasi-steady Analysis of a Morphing Foil

We assume that each section can move independently from the others (Fig. 5a), such that every blade section can be optimised separately. The section angular position is determined by balancing the moments acting along its pitch axis. There are two moments that compete to determine the angular position of a blade section: the reaction of the spring

$$M_{\mathrm{s}}^{\mathrm{2D}} = -\kappa^{\mathrm{2D}}\theta, \tag{12}$$

where θ is the spring strain and κ^{2D} is the spring stiffness of a 2D section, and the hydrostatic pitching moment

$$M_{\mathrm{qs}}^{\mathrm{2D}} = \frac{1}{2}\rho_w U^2 c^2 C_M(\alpha). \tag{13}$$

The blade pitches around the point at the chordwise coordinate $\hat{x}_A = 0.1c$ from the leading edge of each section. The moment coefficient C_M is obtained from the quarter-chord moment coefficient $C_{M_{1/4}}$ by adding the moment contributions of lift and drag with respect to the pitch axis position $\hat{x}_A$, and is computed as

$$C_M(\alpha) = -C_{M_{1/4}} - \left(\frac{1}{2} + \frac{d}{b}\right)\frac{1}{2}\left[C_L\cos(\alpha) + C_D\sin(\alpha)\right], \tag{14}$$

where the location of the pitch axis is indicated with d (following Theodorsen's notation [21]), such that the distance of the pitch axis from the mid-chord is $d = -0.8b$, where $b = {}^{c}/_{2}$. C_M is positive in the clockwise direction according to the sign convention in Fig. 4.

Since the passively controlled system works around the average flow condition for the rigid turbine (*i.e.* $\alpha(t) \approx \overline{\alpha}$), the hydrostatic pitching moment is linearised as

$$C_M(\alpha) = C_{M,0} + C_{M,\alpha}\alpha, \tag{15}$$

where $C_{M,0}$ and $C_{M,\alpha}$ are the best fitting linear regression coefficients of Eq. 14 over a 6 deg range of angle of attacks (*i.e.* $\alpha \in [\overline{\alpha} - 3\,\text{deg}\,,\, \overline{\alpha} + 3\,\text{deg}]$). Equations 13 is thus rewritten as

$$M^{\text{2D}}_{\text{qs}} = \frac{1}{2}\rho_w U^2 c^2 \big[C_{M,\alpha}\alpha + C_{M,0}\big]. \tag{16}$$

The quasi-steady equations for the foil in Fig. 4 are

$$\begin{cases} M^{\text{2D}}_{\text{s}} + M^{\text{2D}}_{\text{qs}} = 0 & \text{(a)} \\ \phi(t) = \beta(t) + \alpha(t) & \text{(b)} \\ \beta(t) = \beta_0 + \delta\theta(t) & \text{(c)} \end{cases} \tag{17}$$

where β is the blade pitch angle and $\delta\theta(t) = \theta(t) - \theta_0$.

The optimisation problem consists in finding the morphing blade that minimises the flapwise bending moment fluctuations on the blade over its revolution, with the requirement that the mean power extracted from the flow is the same as for the rigid turbine. For a 2D foil, the condition on the average power is restricted to the power generated by a single section of the blade and we attempt to minimise the fluctuations of the thrust acting on the section ΔC^{2D}_T, as it ultimately contributes to the fluctuations of the flapwise bending moment. Hence, in 2D the optimisation problem is

$$\begin{aligned} &\min_{\kappa^{\text{2D}}} \hat{J}(\kappa^{\text{2D}}) = \Delta C^{\text{2D}}_T \\ &\quad \text{s.t.} \quad \frac{\partial \overline{C}^{\text{2D}}_P}{\partial \kappa^{\text{2D}}} = 0, \end{aligned} \tag{18}$$

where

$$\overline{C}^{\text{2D}}_P = \frac{1}{2\pi}\int_0^{2\pi} C^{\text{2D}}_P \,\mathrm{d}\,\psi. \tag{19}$$

The problem is solved using an exhaustive search algorithm.

We approximate the average power extracted with the power generated by average flow conditions, namely $\overline{C}_P \approx C_P\left(\overline{\alpha}, \overline{U}\right)$. The average flow conditions $\alpha(t) = \overline{\alpha}$ and $U(t) = \overline{U}$, thus constant power generation, are achieved for a constant pitch angle $\beta(t) = \beta_0$. The requirement, $\beta(t) = \beta_0$, is satisfied with a spring extended by $\theta(t) = \theta_0$ where

$$\theta_0 = \frac{1}{2}\rho_w \overline{U}^2 c^2 \left(\frac{C_{M,\alpha}\overline{\alpha} + C_{M,0}}{\kappa^{2\mathrm{D}}}\right). \tag{20}$$

θ_0 will be referred to as the preload of the spring. The angle of attack is evaluated from the Eq. 17a where the expression for θ is obtained by combining Eq. 17c with $\delta\theta = \theta - \theta_0$. The expression for α is then rearranged to

$$\alpha(t) = \frac{\kappa^{2\mathrm{D}}\left(\phi(t) - \beta_0 + \theta_0\right) - \frac{1}{2}\rho_w c^2 U^2 C_{\mathrm{M},0}}{\kappa^{2\mathrm{D}} + \frac{1}{2}\rho_w c^2 U^2 C_{\mathrm{M},\alpha}}. \tag{21}$$

It's noted that the equation for α is consistent with the definition of the angle of attack for a fixed foil, in fact

$$\lim_{\kappa^{2\mathrm{D}} \to \infty} \alpha = \phi - \beta_0. \tag{22}$$

The spring deformation θ is evaluated by substituting Eq. 17c in Eq. 17b, such that

$$\theta(t) = \phi(t) - \alpha(t) - \beta_0 + \theta_0. \tag{23}$$

For a given value of κ, all the required quantities can be computed and the loads are assessed.

The results for a 2D section will be shown over a range of the non-dimensional spring stiffness

$$\Gamma = \frac{\kappa^{2\mathrm{D}}}{\rho_w c^2 \overline{U}^2}. \tag{24}$$

Γ is the ratio between the two-dimensional stiffness and a representative hydrodynamic moment. The latter is taken as the product of the hydrodynamic force $\rho_w \overline{U}^2 c$ and the arm c.

2.4. Quasi-steady Analysis of the Morphing Blade

In this section, we study a morphing blade where the blade deflection at every spanwise position is the same. The blade morphing is seen as a rigid rotation around the pitch axis and its flexibility is modelled as a torsional spring mounted at the root of the blade (Fig. 5b). We study the impact of the proposed passive pitch system for a rigid blade pitching around an axis at the chordwise coordinate $\hat{x}_A = 0.1c$, rotating at the optimal tip speed ratio $\lambda_0 = 4.5$ for a far-field speed $U_{\mathrm{hub}} = 2$ m s^{-1} at the hub height z_{hub}. The pitching equilibrium is again dictated by the spring reaction and by the hydrostatic loads. The spring acts as a lumped, flexible connection between the blade and the hub and its moment reaction is

$$M_{\mathrm{s}} = -\kappa\theta. \tag{25}$$

The hydrostatic moment M_{qs} takes into account the sum of the moments applied on each i-th section of the blade, and is computed as

$$M_{\mathrm{qs}} = \sum_i \frac{1}{2}\rho_w U_i(t)^2 c_i^2 C_{M_i}(\alpha_i)\delta r_i. \tag{26}$$

The quasi-steady equations that describe the motion of the blade are

$$\begin{cases} M_{\mathrm{s}} + M_{\mathrm{qs}} = 0 & \text{(a)} \\ \phi_i(t) = \beta_i(t) + \alpha_i(t) & (\mathrm{b}_i) \\ \beta_i(t) = \beta_{0_i} + \delta\theta(t) & (\mathrm{c}_i) \end{cases} \tag{27}$$

The optimisation problem is stated similarly to the 2D section case. However, since the entire blade is considered, the minimisation is imposed on the out-of-plane blade root bending moment coefficient C_{RBM}, whereas the constraint considers the power generated by the entire blade. The optimisation problem is stated as

$$\min_{\kappa} \hat{J}(\kappa) = \Delta C_{\mathrm{RBM}}$$
$$\text{s.t.} \quad \frac{\partial \overline{C}_P}{\partial \kappa} = 0 \tag{28}$$

where

$$\overline{C}_P = \frac{1}{2\pi} \int_0^{2\pi} C_P(\psi) \,\mathrm{d}\,\psi, \tag{29}$$

and ΔC_{RBM} is the amplitude of $C_{\mathrm{RBM}} = M_{\mathrm{RB}} / \left(\frac{1}{2} \rho_w U_{\mathrm{hub}}^2 RA \right)$, with $M_{\mathrm{RB}} = \sum_i r_i T_i^{\mathrm{2D}} \delta r_i$ the blade root out-of-plane bending moment.

The optimisation problem is solved using an exhaustive search approach.To meet the requirement of constant power extracted, the spring preload is computed similarly to the two-dimensional case as

$$\theta_0 = \frac{1}{\kappa} \sum_i \frac{1}{2} \rho_w \overline{U}_i^2 c_i^2 (C_{M_i,\alpha} \overline{\alpha}_i + C_{M_i,0}) \delta r_i. \tag{30}$$

By combining Eq. 27 with $\delta\theta = \theta - \theta_0$ we compute the spring deformation θ at each time step as

$$\theta(t) = \frac{\sum_i \frac{1}{2} \rho_w c_i^2 U_i^2 \left(C_{M_i,\alpha} \left(\phi(t) - \beta_0 + \theta_0 \right) + C_{M_i,0} \right) \delta r_i}{\kappa + \sum_i \frac{1}{2} \rho_w c_i^2 U_i^2 C_{M_i,\alpha} \delta r_i}. \tag{31}$$

Then, using the complementarity of angles (Eqs. $27\mathrm{b}_i, \mathrm{c}_i$), the angle of attack is determined as

$$\alpha_i(t) = \phi_i(t) - \beta_{0_i} - \theta + \theta_0. \tag{32}$$

Using the above equations for θ and α and the preload θ_0, all the loads acting on the blade can be computed.

2.5. Dynamic Analysis of the Morphing Blade

We consider a hollow blade made of composite layers then filled with water [22]. The inertia J^{2D} of each blade section is obtained by

$$J^{2D} = \rho_s \int_{\Omega_s} \overline{\boldsymbol{AB}}^2 d\Omega + \rho_w \int_{\Omega_w} \overline{\boldsymbol{AB}}^2 d\Omega, \tag{33}$$

where ρ_s and ρ_w are the density of the blade shell and the density of water respectively, Ω_s is the area of the blade shell on the section, Ω_w is the area occupied by the water within and $\overline{\boldsymbol{AB}}$ represents the relative position of a generic section element from the pitching axis (Fig. 6). A blade usually presents a box spar placed near the pitch axis. Such spar has little influence on the blade inertia, it becomes relevant only for structural consideration, and it is therefore neglected. The inertia J of the entire blade is then computed as

$$J = \sum_i J_i^{2D} \delta r_i, \tag{34}$$

for $i = 1...N$, with N the number of equally spaced blade sections.

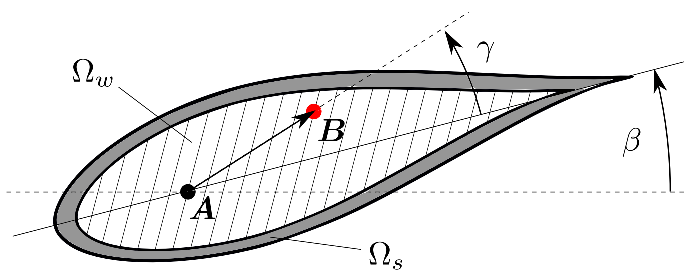

Figure 6: The blade is composed by a composite shell filled with water.

The blade rotates around the rotor axis with angular velocity ω. This leads to the Euler force $\boldsymbol{F}_{\mathrm{Eu}} = -m\frac{d\boldsymbol{\omega}}{dt} \wedge \boldsymbol{r}$, the Coriolis force $\boldsymbol{F}_{\mathrm{Co}} = -m\boldsymbol{\omega} \wedge \frac{d\boldsymbol{r}}{dt}$ and the centrifugal force $\boldsymbol{F}_{\mathrm{c}} = -m\boldsymbol{\omega} \wedge (\boldsymbol{\omega} \wedge \boldsymbol{r})$. In this case, the Euler force disappears because we consider a constant rotation rate ($\frac{d\boldsymbol{\omega}}{dt} = 0$). The Coriolis force is also equal to zero because solid points on the blade do not move radially ($\frac{d\boldsymbol{r}}{dt} = 0$). Conversely, there is a component of $\boldsymbol{F}_{\mathrm{c}}$ that lies in the section plane which generates a pitching moment (Fig. 7). For a generic point $\boldsymbol{B}$ on a blade section, this force, $\boldsymbol{F}_{\mathrm{c}}^B$, generates a moment $\boldsymbol{M}_{\mathrm{c}}^B = \overline{\boldsymbol{AB}} \wedge \boldsymbol{F}_{\mathrm{c},\psi}^B$ that tends to align the blade with the rotor plane.

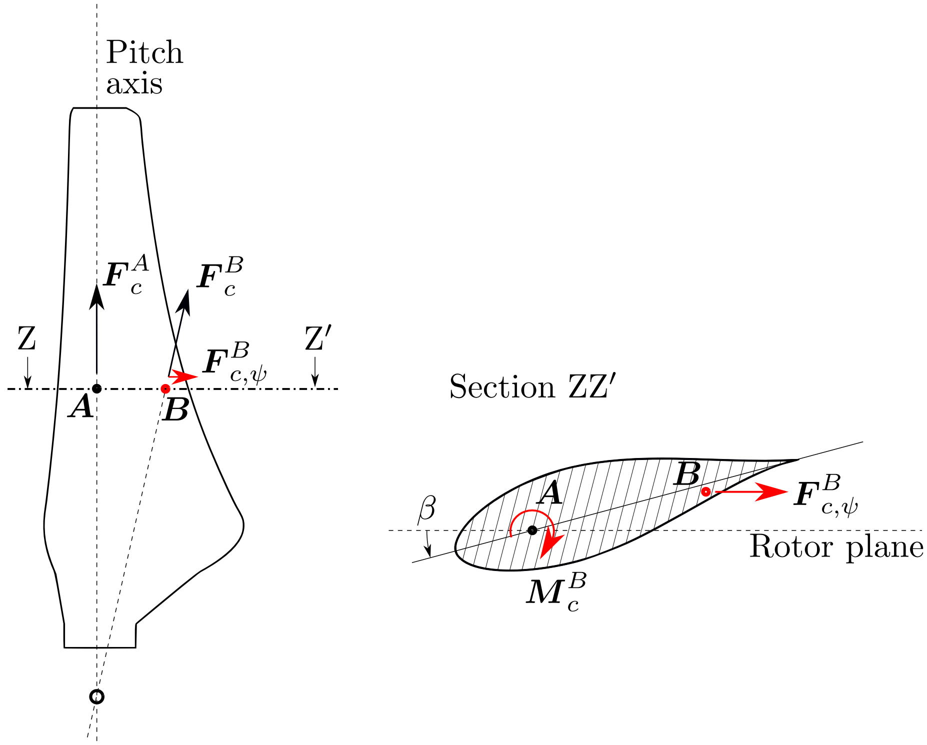

Figure 7: A generic small element of a section that does not lie on the pitch axis is subjected to a centrifugal moment $\boldsymbol{M}_{\rm c}^B$.

The centrifugal moment is evaluated for each section as

$$\begin{aligned} M_{\rm c}^{\rm 2D}(\beta) = &-\frac{1}{2}\omega^2\rho_s\int_{\Omega_s}\overline{\boldsymbol{AB}}^2\sin(2(\beta+\gamma))\,{\rm d}\,\Omega \\ &-\frac{1}{2}\omega^2\rho_w\int_{\Omega_s}\overline{\boldsymbol{AB}}^2\sin(2(\beta+\gamma))\,{\rm d}\,\Omega, \end{aligned} \tag{35}$$

where $\beta+\gamma$ is the angular distance of a blade element from the rotor axis (Fig. 6).

A Taylor-Young first-order expansion is used to approximate the centrifugal moment as

$$M_{\rm c}^{\rm 2D} \approx M_{\rm c}^{\rm 2D}(\beta_0) + \frac{\partial M_{\rm c}^{\rm 2D}}{\partial\beta}\delta\beta. \tag{36}$$

This approximation is valid as long as $\beta \approx \beta_0$, a condition that is met by imposing the requirement of constant power generated (Eq. 28). By construction, $\delta\beta \equiv \delta\theta$ (Fig. 4). Hence, Eq. 36 is rearranged to make explicit the dependency of the centrifugal moment to the spring deformation. The centrifugal moment acting on the entire blade is

$$M_{\mathrm{c}} \approx \sum_i \left(M_{\mathrm{c}_i,0} + M_{\mathrm{c}_i,\theta}\delta\theta\right)\delta r_i, \tag{37}$$

where $M_{\mathrm{c},0} = M_{\mathrm{c}}^{\mathrm{2D}}(\beta_0)$ and $M_{\mathrm{c},\theta} = \frac{\partial M_{\mathrm{c}}^{\mathrm{2D}}}{\partial\theta}$.

The preload angle is computed for average flow conditions, and pitch angle $\beta(t) = \beta_0$. Under these conditions, the centrifugal moment is the only dynamic contributions to the preload angle. Equation 30 is thus modified as

$$\theta_0 = \frac{1}{\kappa}\sum_i \left[\frac{1}{2}\rho_w \overline{U}_i^2 c_i^2 (C_{M_i,\alpha}\overline{\alpha}_i + C_{M_i,0}) + M_{\mathrm{c}_i,0}\right]\delta r_i. \tag{38}$$

A detailed calculations of the centrifugal and inertial terms on a rotating blade can be found in Lanczos [23].

The contribution of the gravity force is neglected. The composite blade shell is filled with water [22], the density of the whole blade is assumed to match that of the surrounding water, and the gravitational force is in equilibrium with the buoyancy force.

2.5.1. Unsteady Hydrodynamics

The oscillations due to the shear flow are periodic but not harmonic, and to estimate the dynamic loads acting on the blade using Theodorsen's theory, we have to consider sinusoidal variations of the angle of attack. We determined the fluctuations of the axial velocity (U_x) such that the angle of attack would fluctuate harmonically with the same amplitude and the same mean value as the inflow oscillations due to the shear profile (Fig. 8). This procedure can be readily extended to generic inflow conditions, where the signal is decomposed in its Fourier harmonic components, and their effects are superimposed via Theodorsen's linear theory. The variations in the angle of attack and in

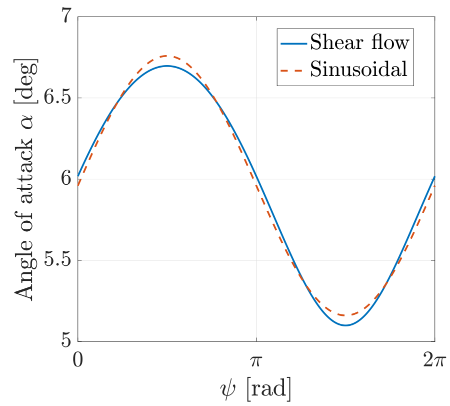

Figure 8: The fluctuations of the angle of attack are approximated by a sinusoidal shape (shown here for $r = 0.75R$).

the axial velocity lead to additional pitching moment contributions. Following Theodorsen [21], the moment on a 2D foil pitching sinusoidally is

$$\begin{aligned} M_{\mathrm{dy}}^{\mathrm{2D}} = \rho_w b^3 \pi & \left[\left(\frac{1}{2} - \frac{d}{b} \right) U \delta\dot{\alpha} + b \left(\frac{1}{8} + \left(\frac{d}{b} \right)^2 \right) \delta\ddot{\theta} \right] \\ & -2\rho_w U b^3 \pi \left(\frac{1}{2} + \frac{d}{b} \right) C(k) \left(\frac{1}{2} - \frac{d}{b} \right) \delta\dot{\theta} \\ & + \frac{1}{2} \rho_w U^2 c^2 C_{M,\alpha} C(k) \delta\alpha \\ & + \frac{1}{2} \rho_w U^2 c^2 \left[C_{M,\alpha} \overline{\alpha} + C_{M,0} \right], \end{aligned} \tag{39}$$

where $\delta\alpha = \alpha - \overline{\alpha}$, $C(k)$ is Theodorsen's circulation function that is expressed in terms of Hankel functions of the reduced frequency $k = \frac{\omega b}{\overline{U}}$. The unsteady pitching moment for the whole blade accounts for the contributions of each section and it is computed as

$$M_{\mathrm{dy}} = \sum_i M_{\mathrm{dy}_i}^{\mathrm{2D}} \delta r_i, \tag{40}$$

The aerodynamic lift L for the quasi-steady analysis accounts only for the hydrostatic loads (Eq. **??**) whereas, in the dynamic analysis, it accounts for both the dynamic and the hydrostatic contributions and is computed as

$$\begin{aligned} L = \pi\rho_w b^2 \left[U\delta\dot{\alpha} - b\left(\frac{d}{b}\right)\delta\ddot{\theta}\right] + 2\pi\rho_w U b^2 C(k)\left(\frac{1}{2} - \frac{d}{b}\right)\delta\dot{\theta} \\ + \frac{1}{2}\rho_w U^2 c\left[C(k)C_L(\alpha) + (1 - C(k))\,C_L(\overline{\alpha})\right]. \end{aligned} \tag{41}$$

The dynamic equations for the blade are

$$\begin{cases} M_\mathrm{s} + M_\mathrm{c} + M_\mathrm{dy} - \mu\delta\dot{\theta} = J\delta\ddot{\theta} & \text{(a)} \\ \phi_i(t) = \beta_i + \alpha_i(t) & (\mathrm{b}_i) \\ \beta_i(t) = \beta_{0_i} + \delta\beta_i(t), & (\mathrm{c}_i) \end{cases} \tag{42}$$

where μ is a parameter that accounts for the mechanical damping of the blade.

The sectional hydrodynamic torque $M^{\mathrm{2D}}_{\mathrm{dy}_i}$ is a function of the average angle of attack $\overline{\alpha}_i$ and of its fluctuations $\delta\alpha_i$ (Eq. 39). Using the complementarity of the angles in Eqs. 42b$_i$ and 42c$_i$, it is possible to express $\delta\alpha_i$ as a function of $\delta\theta$, and to obtain an expression for the blade hydrodynamic torque in Eq. 40 which depend only on $\delta\theta$ and its first and second time derivative. By substituting Eqs. 25, 37, 40 into Eq. 42a, the morphing blade dynamic equilibrium is formulated as:

$$\begin{aligned} \left(J - \sum_i I_{\mathrm{am}_i}\delta r_i\right)\delta\ddot{\theta} + \left(\mu + \sum_i \left(C^{nc}_{\mathrm{am}_i} - C^{c}_{\mathrm{am}_i}\right)\delta r_i\right)\delta\dot{\theta} \\ + \left(\kappa + \sum_i \left(K_{\mathrm{am}_i} - M_{\mathrm{c}_i,\theta}\right)\delta r_i\right)\delta\theta \\ = \sum_i \left(C^{nc}_{\mathrm{am}_i}\delta\dot{\phi}_i + K_{\mathrm{am}_i}\delta\phi_i + M^{\mathrm{2D}}_{\mathrm{qs}_i}(\overline{\phi}_i - \beta_{0_i}) + M_{\mathrm{c}_i,0}\right)\delta r_i - \kappa\theta_0, \end{aligned} \tag{43}$$

where

$$
\begin{aligned}
I_{\text{am}} &= \rho_w b^4 \pi \left(\frac{1}{8} + \left(\frac{d}{b} \right)^2 \right), \\
C^c_{\text{am}} &= -\rho_w U b^3 \pi \left(\frac{1}{2} - \frac{d}{b} \right) \left(1 + 2\frac{d}{b} \right) C(k), \\
C^{nc}_{\text{am}} &= -\rho_w U b^3 \pi \left(\frac{1}{2} - \frac{d}{b} \right), \\
K_{\text{am}} &= \frac{1}{2} \rho_w U^2 c^2 C_{M,\alpha} C(k), \\
M^{\text{2D}}_{\text{qs}_i}(\overline{\alpha}) &= \frac{1}{2} \rho_w U^2 c^2 \left[C_{M,\alpha} \overline{\alpha} + C_{M,0} \right],
\end{aligned}
\tag{44}
$$

The fluctuations are defined by $\delta\phi = \frac{\Delta\phi}{2}\exp(j\omega t)$ and $\delta\alpha = \frac{\Delta\alpha}{2}\exp(j\omega t)$, where $\Delta\phi$ and $\Delta\alpha$ represent the amplitude of the fluctuations of the respective angles and j is the imaginary unit. The blade is expected to oscillate with the same period, namely $\delta\theta = \frac{\Delta\theta}{2}\exp(j\omega t + \chi)$. By substituting $\delta\dot{\theta} = j\omega\delta\theta$, $\delta\ddot{\theta} = -\omega^2\delta\theta$, $\delta\dot{\phi} = j\omega\delta\phi$ and $\delta\ddot{\phi} = -\omega^2\delta\phi$, Eq. 43 is rewritten as

$$
\begin{aligned}
&\Bigg[-\omega^2 \left(J - \sum_i I_{\text{am}_i} \delta r_i \right) + j\omega \left(\mu + \sum_i \left(C^{nc}_{\text{am}_i} - C^c_{\text{am}_i} \right) \delta r_i \right) \\
&\qquad + \left(\kappa + \sum_i \left(K_{\text{am}_i} - M_{\text{c}_i,\theta} \right) \delta r_i \right) \Bigg] \delta\theta \\
&= \sum_i \left(\left(j\omega C^{nc}_{\text{am}_i} + K_{\text{am}_i} \right) \delta\phi_i + M^{\text{2D}}_{\text{qs}_i}(\overline{\phi}_i - \beta_{0_i}) + M_{\text{c}_i,0} \right) \delta r_i - \kappa\theta_0.
\end{aligned}
\tag{45}
$$

The dynamics of $\delta\theta$ are determined by the algebraic solution of Eq. 45 for each time step and the equilibrium position of the blade is computed as $\theta = \theta_0 + \delta\theta$. The solution method is inspired by the work of Medina and Hemati [24].

The optimisation problem is defined as for the quasi-steady case (Eq. 28), where the loads account for the unsteady contributions described in Eq. 41. The angle of attack is determined as for the quasi-steady analysis using Eq. 32, hence all the loads acting on the blade can be computed.

In the Results (Sections 6.2, 6.3), we present the spring stiffness κ and the material damping μ in terms of the nondimensional coefficients

$$\begin{aligned} C_\kappa &= \frac{\kappa}{\rho_w U_{\text{hub}}^2 A c}, \\ C_\mu &= \frac{\mu}{\rho_w U_{\text{hub}} A c^2}. \end{aligned} \tag{46}$$

Akin to Γ, also C_κ and C_μ are made nondimensional using a hydrodynamic force and the length scale c. Here, the force is that acting on the rotor disk and it is proportional to $\rho_w U_{\text{hub}}^2 A$. It is noted that both the coefficients are based on the force on the rotor disk and do not account for the hydrodynamic force associated with the tangential velocity. Hence, as the tip speed ratio increases, the optimum κ and C_κ are expected to increase to match the higher hydrodynamic force associated with the rotation.

3. Real inflow conditions

For this numerical study, we use a flow sample measured at EMEC during a flood tide on November 22nd 2014. This sample was originally chosen by Scarlett *et al.* [3] to investigate numerically the unsteady hydrodynamic response of the Tidal Generation Limited (TGL) turbine subjected to large waves and opposing current. The significant wave height in the sample is 4.2 m, the maximum observed height is about 5 m, and the wave period is 10 s. The turbine is operating at the optimal tip speed ratio 4.5, the magnitude of the inflow speed averaged over the area and the sample time period is 2.77 m s^{-1}, and the rotational speed of the turbine is $\omega = 1.38$ rads^{-1}. Figure 9 shows the time history of the angle of attack at the blade spanwise position $r/R = 0.75$, over 10 rotational periods ($T_r = 2\pi/\omega$). Further details about the measured flow conditions and the measurement system are found in Scarlett *et al.* [3].

The blade deflection at every spanwise position is computed as described in Section 2.4, the blade flexibility is modelled as a torsional spring mounted at the root, and the blade pitches around an axis at the chordwise coordinate $\hat{x}_A = 0.1c$. The pitching equilibrium is described using the quasi-steady analysis

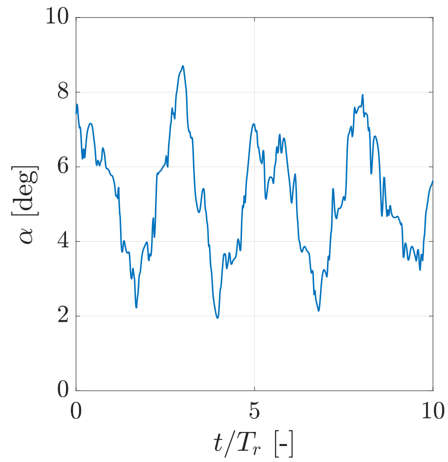

Figure 9: Time history of the angle of attack at $r/R = 0.75$. Data from ReDAPT project re.

in Eq. 27. The optimisation problem is defined in Eq. 28 and solved using an exhaustive search algorithm varying the input spring stiffness. For any stiffness, the preload is computed using Eq. 30. The optimum is represented by the stiffness and preload that minimise the fluctuations of the out-of-plane blade root bending moment C_{RBM}, whilst keeping constant the average power generated by the turbine.

4. Input parameters

The aerodynamics (C_L, C_D) for the blade sections profiles is taken from Gretton and Ingram [25] for a Reynolds number $\mathrm{Re} = 3 \times 10^6$ which matches the flow on a full-scale tidal turbine. The shape of the blade sections is the NACA $63_{(318)} - 4xy$, based on the NACA 6−series designation given by, for instance, Abbott and Von Doenhoff [26]. The thickness xy in percentage of the foil chord varies from the NACA $63_{(318)} - 455$ near the root to the NACA $63_{(318)} - 418$ at the blade tip. An overview of the blade geometry is showed in Fig. 10 and data is provided in Table 1. The blades are thicker at the root, which results in a smooth force variation near the stall angle. For the blade sections with thickness up to 40%, the foil characteristics are interpolated from the data provided by Gretton and Ingram [25]. Instead, for thicker sections, the C_L and C_D of the 40%-thick section are used. This approximation will not affect the results significantly since the root of the blade does not contribute much to the power extraction compared to the mid span and the tip.

The quarter-chord pitching moment $C_{M_{1/4}}$, which is not provided by Gretton and Ingram [25], is taken from Abbott and Von Doenhoff [26] for a NACA $63_3 - 418$ (Fig. 11). The parameters used in the simulations are resumed in Table 2.

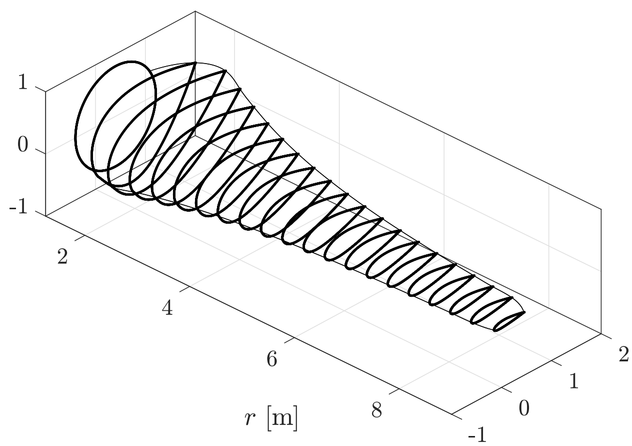

Figure 10: TGL blade geometry adapted from Gretton and Ingram [25].

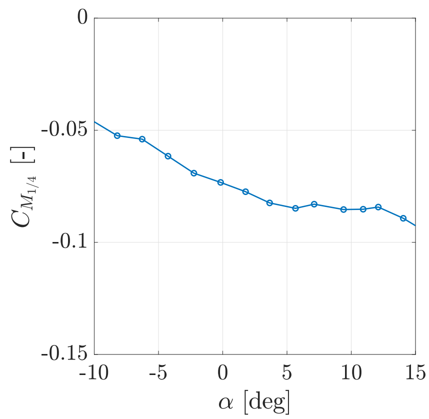

Figure 11: Quarter chord pitching moment coefficient for a NACA $63_3 - 418$ as a function of α, at Re $= 3 \times 10^6$. Data taken from Abbott and Von Doenhoff [26].

5. Code Validation

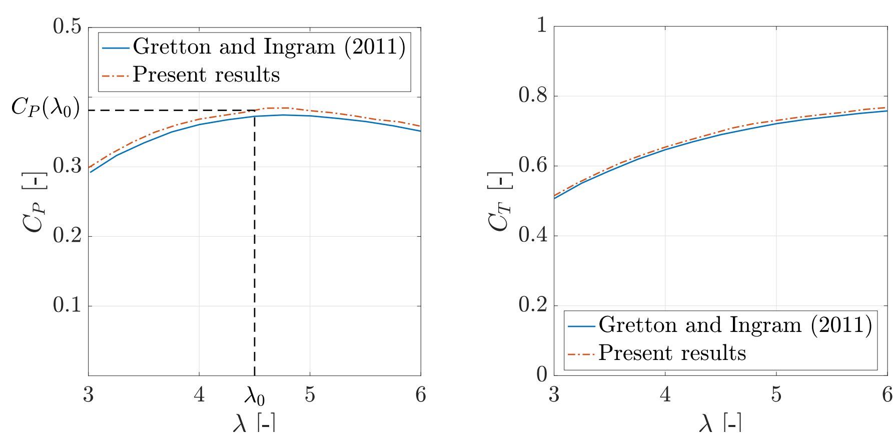

(a) Power coefficient

(b) Thrust coefficient

Figure 12: Comparison of the BEMT results of this study and the CFD results from Gretton and Ingram [25] using $U_{\text{hub}} = 2$ m s^{-1}. C_P and C_T refer to the entire turbine.

First, we assess the accuracy of the numerical code for a turbine subjected to steady flow conditions, against the data from Gretton and Ingram [25],

Radius [m]	Twist [deg]	Chord [m]	Thickness ratio	Profile
1.25	32.5	1.612	1.000	Circle
2.05	23.2	2.271	0.550	$63_{(318)} - 455$
2.45	19.9	2.119	0.533	$63_{(318)} - 453$
2.85	17.2	1.962	0.511	$63_{(318)} - 451$
3.25	14.9	1.813	0.485	$63_{(318)} - 449$
3.65	13.1	1.677	0.454	$63_{(318)} - 445$
4.05	11.5	1.556	0.422	$63_{(318)} - 442$
4.45	10.2	1.447	0.390	$63_{(318)} - 439$
4.85	9.1	1.351	0.359	$63_{(318)} - 436$
5.25	8.1	1.265	0.330	$63_{(318)} - 433$
5.65	7.2	1.189	0.306	$63_{(318)} - 431$
6.05	6.4	1.120	0.286	$63_{(318)} - 429$
6.45	5.8	1.058	0.275	$63_{(318)} - 427$
6.85	5.2	1.003	0.267	$63_{(318)} - 427$
7.25	4.6	0.953	0.255	$63_{(318)} - 426$
7.65	4.2	0.907	0.243	$63_{(318)} - 424$
8.05	3.7	0.865	0.227	$63_{(318)} - 423$
8.45	3.3	0.827	0.208	$63_{(318)} - 421$
8.85	3.0	0.792	0.188	$63_{(318)} - 419$
9	2.8	0.600	0.180	$63_3 - 418$

Table 1: Blade geometry.

who studied a full-scale turbine prototype from TGL at different tip speed ratio λ, where the free stream velocity is uniform with $U_\infty(z) = U_{\text{hub}}$ and $U_x = U_\infty(1-a)$. We compare the thrust and power coefficients in Fig. 12. The difference of the computed power coefficient with the CFD data from Gretton and Ingram [25] is always smaller than 3%, whereas the thrust differs by less

	Blade section	
	$r = 0.5R$	$r = 0.75R$
Mean angle of attack $\overline{\alpha}$ [deg]	9.58	5.96
Twist angle β_0 [deg]	10.17	5.39
Chord c [m]	1.445	1.019
Foil type	NACA $63_{(318)}439$	NACA $63_{(318)}427$
Axial induction factor a [-]	0.1835	0.3112
Tangential induction factor a' [-]	0.0182	0.0164
Mean inflow speed $\overline{U}$ [m s^{-1}]	4.82	6.98
Blade length R [m]	9	
Far field flow speed U_{hub} [m s^{-1}]	2	
Hub height z_{hub} [m]	20	
Pitch axis position $\hat{x}_A/c$ [-]	0.1	
Rotational speed ω [rad s^{-1}]	1	
Blade shell thickness [mm]	56.5 (root) - 14.5 (tip)	
Blade shell density ρ_{s} [kg m^{-3}]	570 (root) - 660 (tip)	
Sea water density ρ_{w} [kg m^{-3}]	1025	

Table 2: Simulation parameters.

than 2% over the considered range $\lambda \in [3, 6]$, including the optimal operating point $\lambda_0 = 4.5$ where we study the performance of the morphing blade.

Next, we consider the accuracy of the model at predicting loads fluctuations when the turbine is subjected to unsteady flow. The predictions of our model are compared to the results of Scarlett *et al.* [3]. They developed a model based on blade element momentum theory coupled with a dynamic stall model, and they validated it against data from AeroDyn, an opensource aerodynamic software developed by NREL, and wind tunnel data. To aid the modelling of dynamic stall phenomena, Scarlett *et al.* [3] considered the blade made of

NREL S814 airfoils, since a large database of empirical dynamic stall parameters is available for a series of NREL airfoils [27]. In particular, the NREL S814 generates a similar power coefficient to the NACA 63-418, which represents the tip airfoil of the TGL turbine blades. Therefore, the comparison is made for the lift experienced by the tip section ($r/R = 1$), over 56 rotational periods. In Fig. 13, we show the time history of the lift coefficient over 5 periods, and also the predictions from Scarlett *et al.* [3] when the turbine with rigid blades is subjected to the real flow conditions, measured at the EMEC tidal test site on November 22nd 2014. Our results match qualitatively both the unsteady and quasi-steady lift from Scarlett *et al.* [3]. The average discrepancies over 56 periods are 6% compared to Scarlett's quasi-steady model, and less than 5% compared to the unsteady model, with maximum deviations of 18% and 40% respectively. Discrepancies with Scarlett's quasi-steady model might be partially due to geometric differences between the two airfoils, as the NREL S814 has double curvature and 3% maximum camber, whereas the NACA 63-418 has simple curvature and 2.2% maximum camber. Bigger differences are noticed against Scarlett's unsteady model, however, these are due to unsteady phenomena and are noticed also between both of Scarlett's models.

There is no experimental data for a turbine with a morphing concept such as that discussed in this paper. Hence, the load predictions are validated for a rigid blade and cannot be validated for the morphing blade. However, Dai *et. al* [28] performed a 2-dimensional CFD investigation of the performance of a passively pitching NACA 63-427, which corresponds to the airfoil at $r/R = 0.75$ of the turbine blade used in the current study. They considered a rigid and an airfoil pitching passively around the axis at $\hat{x}_A = 0.1c$ and subjected to a periodically varying inflow speed representing a blade rotating in shear flow. The passive pitch was modelled with an akin mass-damper-spring system to that in this paper. The CFD predicted a reduction of the amplitude of the load fluctuations within 7% of the predictions of the present analytical model (Fig. 14).

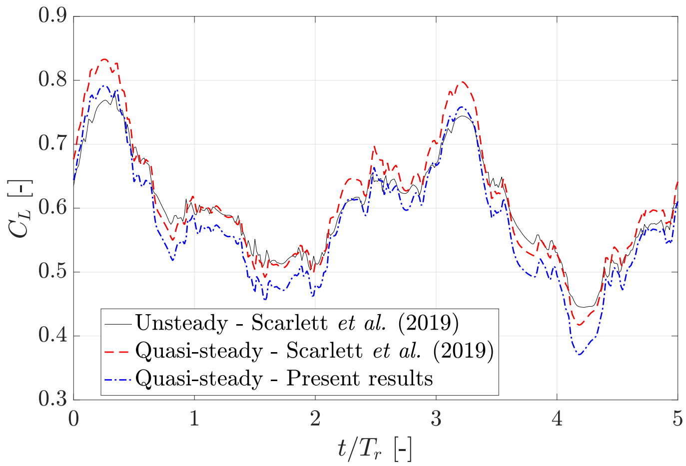

Figure 13: Comparison of lift coefficient between Scarlett *et al.* [3] unsteady results (black line), quasi-steady results (red dashed line), and present quasi-steady results (blue dashed-dotted line).

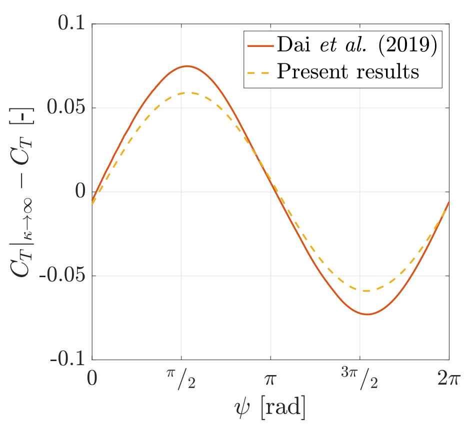

Figure 14: Comparison of CFD and analytical results showing the difference of C_T between rigid and morphing blades.

6. Results

6.1. Quasi-steady Analysis of a Morphing foil

The results for the passive pitch control applied to a 2D foil are presented here. Figure 15 shows the evolution of $\alpha(t)$ and $C_T^{2\text{D}}(t)$ for the foil at $r = 0.5R$ over the azimuthal coordinate ψ (Fig. 1), whereas Fig. 16 refers to the blade section at $r = 0.75R$. Both cases show the fluctuations over one revolution of the foils equipped with springs that are optimised to mitigate the thrust fluctuations for the respective flow conditions (Table 3). The non-dimensional stiffness Γ is defined as the ratio between spring stiffness κ and the hydrostatic stiffness $\rho_w c^2 \overline{U}^2$ (Eq. 24), and Γ_0 is the optimal value. On both blade sections, the thrust fluctuations are almost perfectly cancelled.

Similar performance can be achieved for any blade section as long as the stiffness and preload are optimised for the flow condition that the section experiences. Therefore, if each section can be equipped with the optimal stiffness and can deflect independently of the neighbouring sections, perfect unsteady load cancellation is possible also for the full blade.

Such optimal behaviour is possible thanks to the angle of attacks that varies in opposition to the fluctuations of the inflow angle. In fact when the inflow angle ϕ reaches a peak value α is at a minimum, as observed by Shen *et al.* [29].

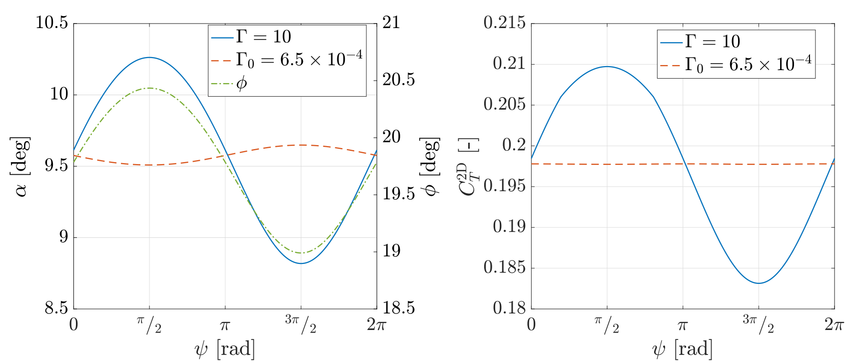

(a) (b)

Figure 15: Section at $r = 0.5R$: evolution of angle of attack (a) and thrust coefficient (b).

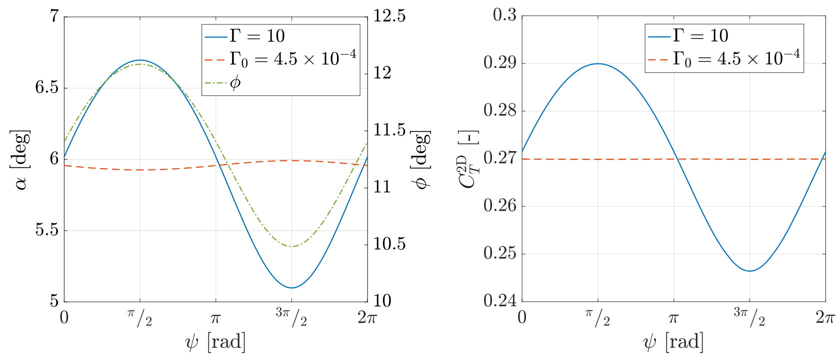

(a) (b)

Figure 16: Section at $r = 0.75R$: evolution of angle of attack (a) and thrust coefficient (b).

	Optimal spring properties		Thrust fluctuations ΔC_T^{2D}	
Blade section	Γ_0 [-]	θ_0 [deg]	% mean C_T^{2D}	% reduction
$r = 0.5R$	6.5×10^{-4}	132	0.03 (13.46)	99.74
$r = 0.75R$	4.5×10^{-4}	233	0.02 (16.12)	99.85

Table 3: Minimum load fluctuations using optimal springs for two blade sections. The number in parenthesis refer to the respective rigid blade sections.

This behaviour is explained in Fig. 17. The loads on the foil change because of the changes in the angle of attack but also in the flow velocity. When the blade is in the upper position, the foil pitches in order to compensate the incidence increase, such that both α and C_T^{2D} are restored to their initial values (Fig. 17b). However, the inflow speed increases as well causing higher hydrostatic moments which further pitch the foil (Fig. 17c). Essentially, the angle of attack is reduced to a value which is lower than its initial value to compensate the increase in the inflow speed. Similarly, when the blade is in the lower position, the foil pitches to a higher incidence in order to cancel the effect of the reduction in the

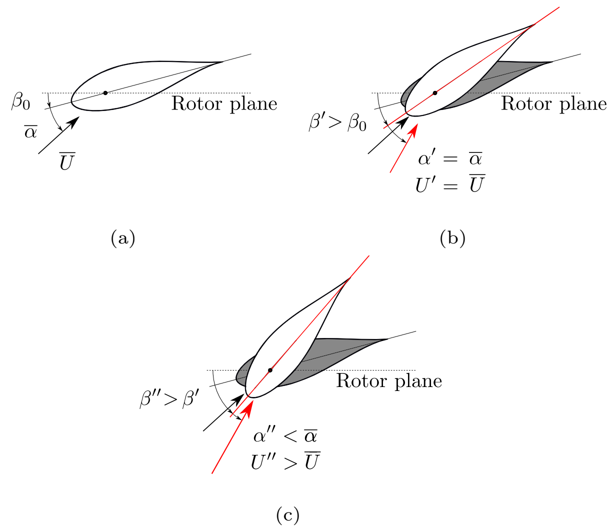

Figure 17: Reaction of the morphing foil to an increase of angle of attack and flow speed; (a) reference condition; (b) effect of the angle of attack only and (c) combined effect of the increase of both the angle of attack and flow speed.

incoming flow speed. Therefore, the spring that minimises the fluctuations of $C_T^{2\mathrm{D}}$ is different from the one that minimises the oscillations of α. In particular, Fig. 18 shows the amplitude of the fluctuations of $C_T^{2\mathrm{D}}$ (top) and α (bottom) for the blade section at $r = 0.75R$, for a range of values of Γ. It's shown that a spring that minimises the fluctuations of α is stiffer than the spring that minimises the fluctuations of $C_T^{2\mathrm{D}}$.

The results for 2D sections are summarised in Fig. 19, which shows the evolution of $C_T^{2\mathrm{D}}$ and $C_P^{2\mathrm{D}}$ during the revolution of the blade section at $r = 0.75R$ for different values of the non-dimensional stiffness Γ. The dotted lines on Fig. 19a show the blade azimuthal position. The maximum value $\Gamma = 10$ represents the condition of a rigid foil, where the spring becomes too stiff to bend and the loads on the section are not effectively alleviated.

In Fig. 19b, the range of Γ is narrowed to focus the reader attention around the optimal value $\Gamma_0 = 4.5 \times 10^{-4}$ which is highlighted by the dotted line. The

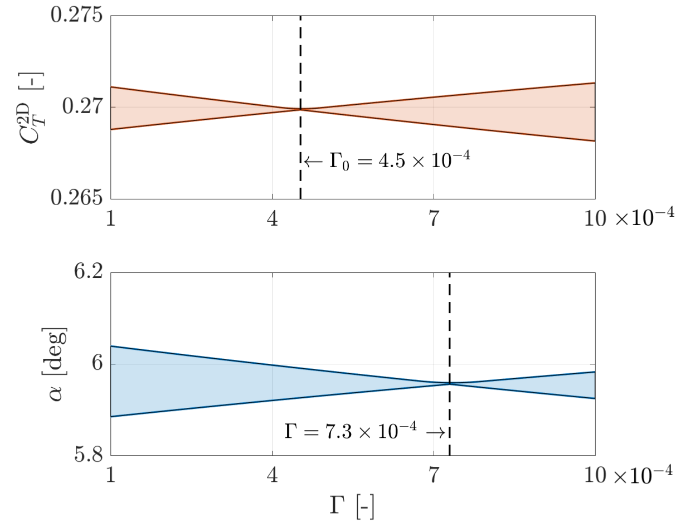

Figure 18: Fluctuations of C_T^{2D} (top) and α (bottom) for the section at $r = 0.75R$, for a range of values of Γ.

optimal stiffness is represented by a slightly curved line. Therefore, the C_T^{2D} still exhibits small fluctuations throughout each revolution, although these fluctuations are negligible compared to the mean value and compared to fluctuations experienced by the rigid foil. The quasi-steady analysis shows that, for very low stiffness values, the variations of the thrust coefficient is reversed. The preload θ_0 is inversely proportional to Γ (Eq. 20), which means that the lower the value of Γ the higher needs to be the preload in order to balance the hydrostatic moment. Therefore, reducing the stiffness of the spring leads quickly to very high values of θ_0. C_P^{2D} always oscillates around the same value whilst the amplitude of the oscillations is slightly reduced.

6.2. Quasi-steady Analysis of the 3D Morphing Blade

The analysis presented in Section 6.1 is extended to the entire blade. A spring with quasi-steady non-dimensional stiffness (Eq. 46) $C_\kappa^{qs} = 6.0 \times 10^{-3}$ and quasi-steady preload angle $\theta_0^{qs} = 313$ deg leads to variations of the thrust

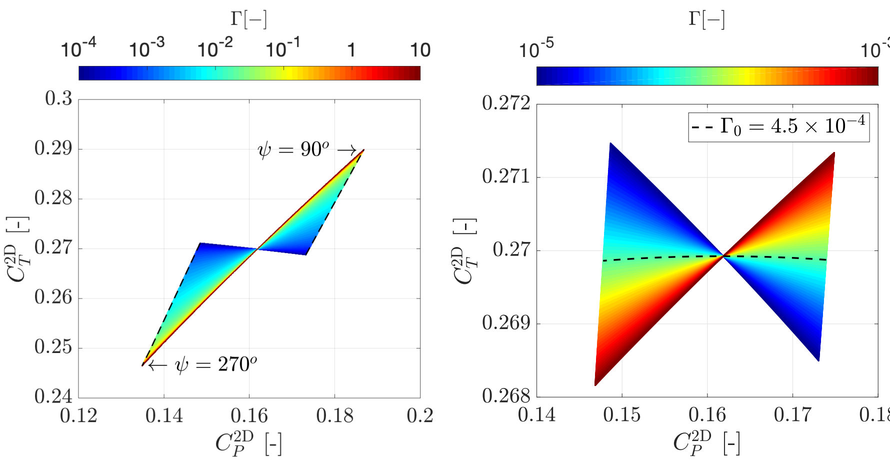

(a) (b)

Figure 19: Variations of the power and thrust coefficients as the inflow angle varies through the rotation of the blade, (a) for a large range of values $\Gamma \in [10^{-5}, 10]$ and (b) around $\Gamma_0 = 4.5 \times 10^{-4}$.

coefficient at each section that are negligible, whilst the mean power generated in one revolution is unaffected. Figure 20 shows the thrust fluctuations over the area swept by the blade for a rigid (Fig. 20a) and a morphing blade (Fig. 20b). In particular, we plot the thrust coefficient of the rigid blade $C_T^{2D}|_{\kappa\to\infty}$ and of the optimal morphing blade C_T^{2D} divided by the maximum sectional thrust of the rigid blade. The load is concentrated in the outer half of the blade and it drops at the tips and towards the hub. The high thrust experienced by the blade when $\psi = 90$ deg (Fig. 20a) is reduced thanks to the blade flexibility, whereas the lower thrust at $\psi = 270$ deg is increased.

The effectiveness of the blade flexibility is finally checked for the flapwise blade root bending moment shown in Fig. 21. Since the changes in the amplitude of the thrust fluctuations for the blade in the upward/downward positions are of opposite sign, the bending moment is kept nearly constant over each revolution. The morphing blade experiences RBM fluctuations with amplitude smaller than 0.5% of the average bending moment. As the amplitude of the fluctuations

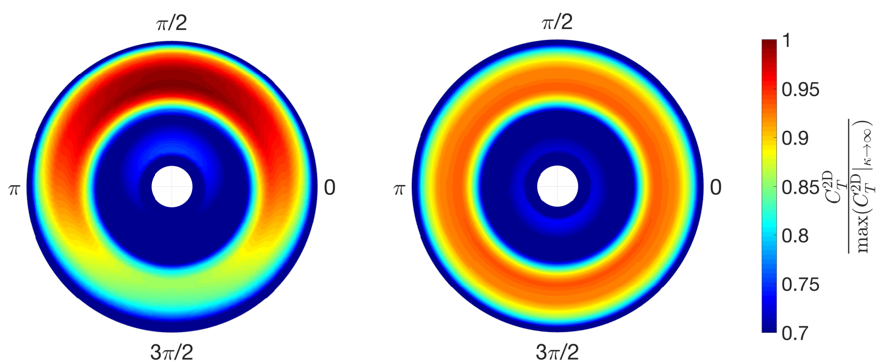

(a) (b)

Figure 20: Map of the thrust coefficient over the rotor disc for (a) a rigid blade and (b) a morphing blade.

on the rigid blade is 18%, the morphing blade mitigated 98% of the RBM fluctuations. Compared to the 2D analysis, the performance is slightly lower. Each section experiences a different load fluctuation amplitude that requires a different blade deflection. As the morphing blade is optimised in a global fashion, it affects mainly the sections that experience stronger load fluctuations, and it is thus sub-optimal for the sections that contribute the least to the blade loads causing a performance reduction.

6.3. Dynamic Analysis of the 3D Morphing Blade

We study to what extent the dynamics of the blade and the unsteadiness of the fluid loads affect the performances of the passive control system. From Eq. 42, we consider the centrifugal moment M_{c}, the hydrodynamic moment M_{dy} and that due to the mechanical damping of the blade $\mu\dot{\theta}$. The blade non-dimensional damping is initially set to $C_\mu = 10^{-3}$ (Eq. 46), which represents a negligible value. Its effect will be discussed in Section 6.4. Figure 22 shows that the effectiveness of the morphing blade in reducing the RBM oscillations is only marginally affected by the blade inertia and the unsteadiness of the flow. Figure 23 shows that the blade inertia and the fluid-induced damping have a small effect on the system effectiveness.

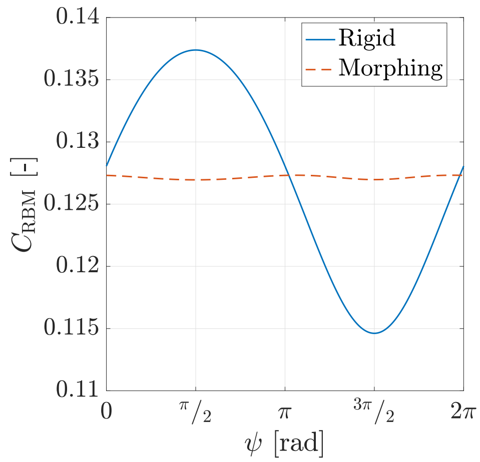

Figure 21: Quasi-steady analysis of the flapwise one-blade root bending moment C_{RBM}. The blade is equipped with a spring with $C_{\kappa}^{\mathrm{qs}} = 6.0 \times 10^{-3}$ and $\theta_0^{\mathrm{qs}} = 313$ deg.

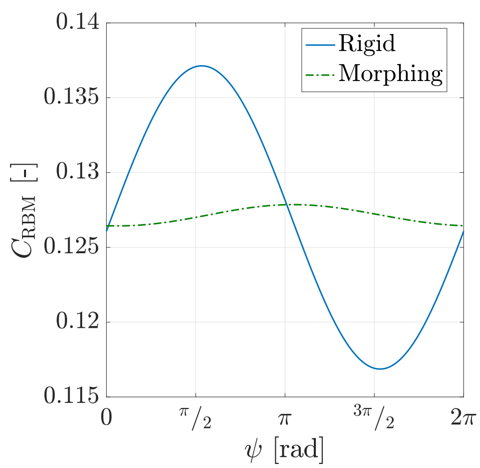

Figure 22: Dynamic analysis of the evolution of C_{RBM}. The blade is equipped with a spring with $C_{\kappa}^{\mathrm{dy}} = 1.1 \times 10^{-2}$ and $\theta_0^{dy} = 171$ deg.

Accounting for the additional moments, we find that the optimal non-dimensional stiffness and preload obtained for the dynamic model are $C_{\kappa}^{\mathrm{dy}} = 1.1 \times 10^{-2}$ and $\theta_0^{\mathrm{dy}} = 171$ deg. The optimal spring is stiffer than the one in the previous sec-

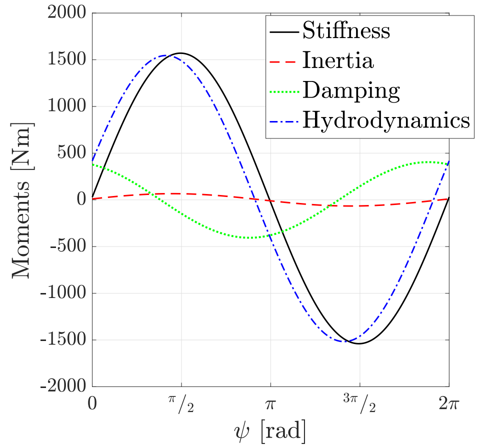

Figure 23: Dynamic contributions to the moment equilibrium of the blade, for $C_\kappa^{\mathrm{dy}} = 1.1 \times 10^{-2}$ and $\theta_0^{dy} = 171$ deg.

tion because of the presence of unsteady loads. Table 4 shows the reduction in the bending moment fluctuations. As the optimal spring for the dynamic case is different than the optimal spring obtained for the quasi-steady model, it is difficult to understand whether the difference in the performance are due to a different spring or to dynamic effects. For ease of comparison, in Table 4 we display two sets of results for the dynamic model and for the quasi-steady one (in parenthesis), both using the same spring optimised for the dynamic model. The performance estimated with the quasi-steady model is slightly lower than before as the spring is suboptimal. The system dynamics affect the blade performance only marginally, as the reduction of RBM fluctuations is only 5% lower compared to the best quasi-steady performance previously shown. It must be noted that the mean power generated is the same as for the rigid blade.

6.4. Effect of Blade Mechanical Damping

In this section, we consider the effects of the mechanical damping μ. Figure 24 shows the reduction of the fluctuations of the bending moment coefficient for a range of values of the stiffness coefficient C_κ and of the damping coefficient

	Optimal spring		RBM fluctuations ΔC_{RBM}	
	C_κ^{dy} [-]	θ_0^{dy} [deg]	% mean C_{RBM}	% reduction
Rigid	–	–	16(18)	–
Morphing	1.1×10^{-2}	171 (177)	2.6 (< 1)	93 (96)

Table 4: Optimal dynamic results for the morphing blade model. The numbers within the parenthesis refer to the quasi-steady analysis that employed the spring optimised for the dynamic case.

C_μ. In particular, the amplitude of the bending moment fluctuation ΔC_{RBM} is divided by the amplitude of the fluctuations for the rigid blade $\Delta C_{\mathrm{RBM}}|_{\kappa\to\infty}$.

The optimal working point for each curve is their minimum. When C_μ is large compared to the hydrodynamic damping, the efficacy of the morphing blade is poor. Conversely, for $C_\mu = 1$ the system performance improves considerably, and the fluctuations of the blade root bending moment are reduced by 98%. Increasing the damping, the lowest point of each curve moves to higher values of C_κ, hence the optimal performance of the passive control system is achieved with stiffer springs. For high values of C_κ, all the curves in Fig. 24 collapse and converge asymptotically to 1. The system is not very sensitive to small changes in the spring stiffness, as the reduction in the ΔC_{RBM} does not vary significantly near the optimum.

The blade does not experience any resonance phenomena, and, even for negligible mechanical damping C_μ, the fluid acts as a damper, the motion of the blade is effectively damped. In fact, by considering the blade damping as a lumped parameter, it is possible to define a damping ratio as

$$\zeta = \frac{C_{\mathrm{tot}}}{2\sqrt{J_{\mathrm{tot}} K_{\mathrm{tot}}}}, \tag{47}$$

where J_{tot}, C_{tot} and K_{tot} represent the inertia, the damping and the stiffness of the system respectively. Similarly, we define the natural frequency of such system as

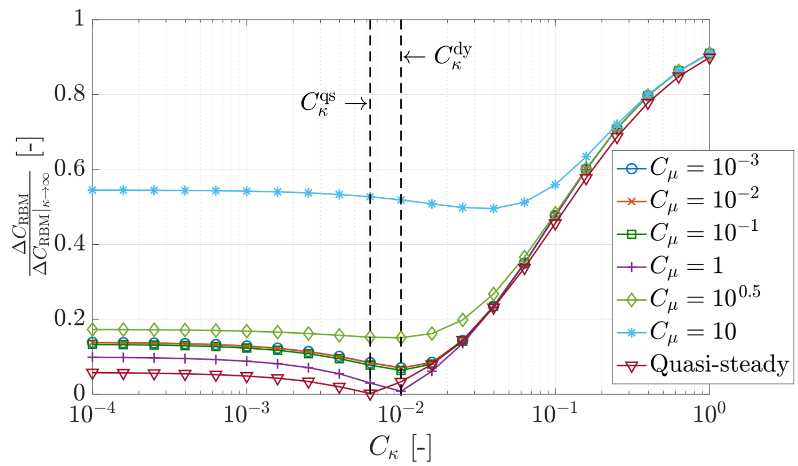

Figure 24: Normalised amplitude of the root bending moment for a range of values of C_κ and C_μ.

$$\Omega_N = \sqrt{\frac{K_{\mathrm{tot}}}{J_{\mathrm{tot}}}}, \tag{48}$$

where J_{tot} is the sum of all the inertial terms in Eq. 43, C_{tot} is the sum of all the terms that multiply $\delta\dot{\theta}$ and K_{tot} is the sum of the terms that multiply $\delta\theta$, the damping ratio describes the coupled mechanical-hydrodynamic system. For the range of values of C_κ considered, the natural frequency of the coupled system is always greater than 2.8 rad/s. Since the frequency of the load fluctuations is $\omega = 1$ rad/s, the blades are likely to experience no resonance. The damping ratio ζ changes with the spring stiffness, and at the minimum of each curve, it always takes values greater than 0.4. Therefore, the hydrodynamic contribution alone dampens the motion of the blade substantially. The effect of the damping can be observed in Fig. 25, which shows the blade motion amplitude $\Delta\theta$ over the same range of C_κ and C_μ. All curves converge for stiff springs, for which $\Delta\theta$ tends to zero. For very flexible springs, $\Delta\theta$ is never higher than 2 deg and it decreases for increasing damping values. On the other hand, the preload θ_0 is inversely proportional to the spring stiffness and increases rapidly from zero to more than 10^4 deg for $C_\kappa < 10^{-4}$.

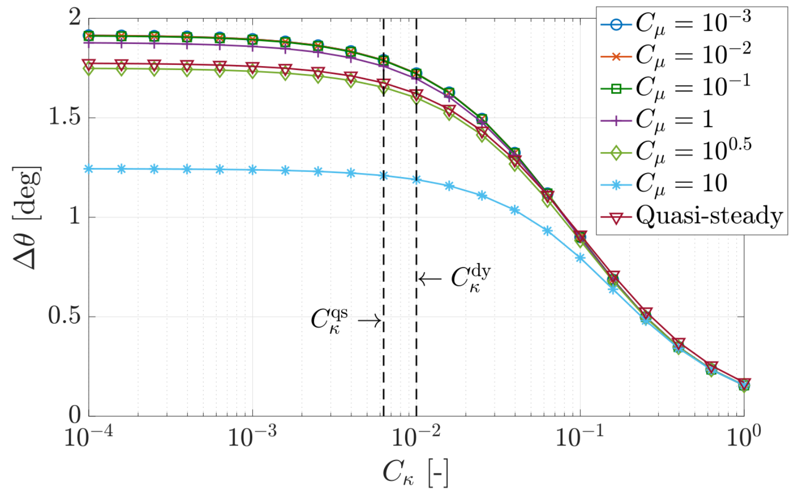

Figure 25: Evolution of $\Delta\theta$ for a range of values of C_κ and C_μ.

6.5. Morphing blade performance in real flow conditions

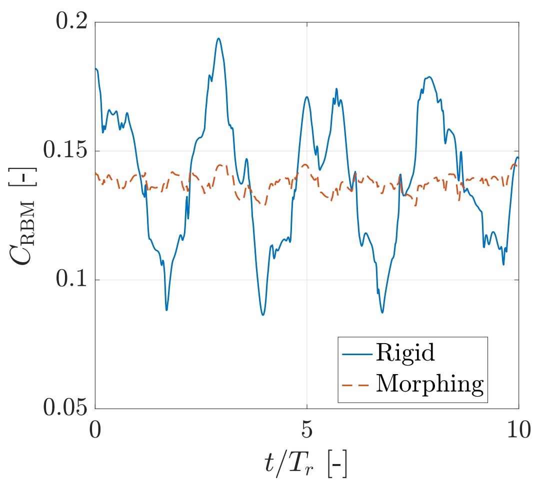

Figure 26: Root bending moment under real flow conditions for a rigid blade (blue line) and a morphing blade (red dashed line).

The performance of morphing blades is estimated again, this time using realistic inflow conditions, measured during a flood tide at the EMEC tidal testing site on the 22nd of November 2014. Figure 26 shows the root bending moment coefficient C_{RBM} simulated over 10 rotational periods, for a rigid blade and a morphing blade that has been optimised to minimise the fluctuation of C_{RBM}. Using a spring with quasi-steady non-dimensional stiffness $C_{\kappa}^{\mathrm{qs}} = 5.1 \times 10^{-2}$, and quasi-steady preload angle $\theta_0^{\mathrm{qs}} = 32$ deg, the fluctuations of the root bending moment are reduced by 82%, whilst the average power coefficient has decreased by 2%. Results are resumed in Table 5.

	Optimal spring		RBM fluctuations ΔC_{RBM}	
	C_{κ}^{qs} [-]	θ_0^{qs} [deg]	% mean C_{RBM}	% reduction
Rigid	–	–	101	–
Morphing	5.1×10^{-2}	32	18	82

Table 5: Optimal morphing blade model when subjected to real flow conditions.

The efficacy of the morphing blade to mitigate the fluctuations induced by real inflow conditions is slightly lower than that shown in Sections 6.2 and 6.3 for a modelled shear flow. The shear flow induces periodic fluctuations at the blade rotational frequency, whereas the real flow conditions induce load fluctuations over a wide range of frequencies. Since the load fluctuations are dominated by the high-amplitude, low-frequency waves, the optimal morphing blade is tuned to operate around that frequency. Therefore, the system is not as effective at alleviating the high-frequency, low-amplitude fluctuations, as shown in Fig. 26.

We have shown that morphing blades are capable of alleviating unsteady load fluctuations caused by shear flow and large waves. In our model, flow fluctuations are experienced by the blade as oscillations of the inflow speed and of the angle of attack, and a morphing blade mitigates the loads by inverting the sign of the angle of attack variations. The mechanism underlying load mitigation by morphing blade is independent of the flow condition. Hence, we believe that similar performance can be achieved for a wide range of unsteady flow conditions, including turbulence, yaw misalignment, wakes of upstream turbines, and the proximity of other devices. As the frequency of the fluctuation increases, such as for small-scale turbulence, the inertia of the blade leads to a reduction of the system efficiency. Moreover, the model is not capable to consider the effect of high-frequency flow fluctuations with a period of the order of $c/(\omega R)$, such that the flow cannot be considered uniform along the chord. In such cases, a more sophisticated model should be used.

7. Conclusions

In this paper we discuss the underlying mechanism by which morphing blades can mitigate unsteady load fluctuations on tidal turbines.

By neglecting mass and damping effects, and by further assuming independent blade sections at any spanwise location, we show that a morphing blade can completely cancel the thrust fluctuations ($> 99\%$ reduction) without affecting the mean torque and thus the energy harvested. This is possible because, when a gust occur, the increased flow speed makes the blade to pitch and this result in a reduction in the angle of attack. The optimum blade flexibility is such that the load increase due to the higher flow speed is cancelled by the load reduction due to the lower angle of attack.

The condition that each blade section deflects independently of those at other spanwise locations is not critical for the effectiveness of the system. The opposite limiting condition is when all blade sections must pitch by the same amount, which is saying that the blade is rigid and has a passive pitching mechanism at the root. In this case, we show that the root bending moment fluctuations are decreased by more than 98% for a 18 m diameter, 1 MW turbine in a sheared tidal current operating at a tip speed ratio of 4.5.

The effectiveness of the system is partially decreased by both the mass and damping of the system.

Accounting for the unsteady hydrodynamics effects and the blade inertia, the root bending moment fluctuations are reduced by more than 93%. Their effect, however, depends on the onset flow conditions. Hence, we also model the morphing blade in the tidal flow conditions measured at the EMEC site with more than 4 m significant wave height with a period of 10 s. In these conditions, the morphing blades enable a root bending moment reduction of more than 82%. Hence, we conclude that unsteady hydrodynamic effects and blade inertia are important, but do not undermine the general effectiveness of the morphing blades.

On the other hand, a high mechanical damping can undermine the ability to mitigate unsteady loads. The damping depends on the design of the morphing blade and can be due to the viscous dissipation of the flexible material, or on the mechanical damping of a passive pitch mechanism. Our parameter study can be used by future researchers to estimate the unsteady load mitigation of different blade design concepts.

This conceptual study does not consider the practicalities arising from the design and manufacturing of a morphing blade. Before this technology can be adopted by the industry, more research is needed to address the need for a new structural design, to identify the materials that can be adopted, and the associated manufacturing and the supply chain. Since tidal turbine blades are typically made of a composite structure reinforced with a boxspar, the use of a novel structure and materials will require extensive testing and characterisation to guarantee reliability and survivability of the blade. Overall this paper contributes by providing insights on the underlying mechanism of morphing blades and the blade behaviour that future designs need to achieve.

Acknowledgements

This work was supported by the EPSRC, grant reference number EP/L016680/1, which funded the PhD scholarship of the first author.

References

References

[1] D. Cagney, R. Gruet, Ocean_Energy_Europe, Powering Homes Today, Powering Nations Tomorrow, Technical Report, ETIP Ocean, 2019.

[2] F. Taveira-Pinto, P. Rosa-Santos, T. Fazeres-Ferradosa, Marine renewable energy, Renewable Energy 150 (2020) 1160–1164.

[3] G. T. Scarlett, B. Sellar, T. van den Bremer, I. M. Viola, Unsteady hydrodynamics of a full-scale tidal turbine operating in large wave conditions, Renewable Energy 143 (2019) 199–213.

[4] G. T. Scarlett, I. M. Viola, Unsteady hydrodynamics of tidal turbine blades, Renewable Energy 146 (2020) 843–855.

[5] B. Murray, S. Leen, C. M. O Bradaigh, Void distributions and permeability prediction for rotationally moulded polymers, J. Mater. Des. Appl. 229 (2015) 403–418. URL: `http://pil.sagepub.com/lookup/doi/10.1177/1464420714525135`. doi:`10.1177/1464420714525135`.

[6] T. Fazeres-Ferradosa, M. Welzel, A. Schendel, L. Baelus, P. R. Santos, F. T. Pinto, Extended characterization of damage in rubble mound scour protections, Coastal Engineering 158 (2020) 103671.

[7] H. Díaz, J. Rodrigues, C. G. Soares, Preliminary assessment of a tidal test site on the minho estuary, Renewable Energy 158 (2020) 642–655.

[8] M. Harrold, P. Ouro, T. O'Doherty, Performance assessment of a tidal turbine using two flow references, Renewable Energy 153 (2020) 624–633.

[9] C. R. Vogel, R. H. Willden, Improving Tidal Turbine Performance Through Multi-Rotor Fence Configurations, J. Mar. Sci. Appl. 18 (2019) 17–25. doi:`10.1007/s11804-019-00072-y`.

[10] F. Scuiller, T. Tang, Z. Zhou, M. Benbouzid, J. Fre, A review of energy storage technologies for marine current energy systems, Renew. Sustain. Energy Rev. 18 (2013) 390–400. doi:10.1016/j.rser.2012.10.006.

[11] T. Barlas, G. van Kuik, Review of state of the art in smart rotor control research for wind turbines, Progress in Aerospace Sciences 46 (2010) 1–27.

[12] T. Barlas, M. Lackner, Smart rotor blade technology applied to the Upwind reference turbine, Sandia National Labs, Alberquerque, USA, 2008.

[13] T. K. Barlas, G. J. van der Veen, G. A. M. Kuik, Model predictive control for wind turbines with distributed active flaps: incorporating inflow signals and actuator constraints, Wind Energy 15 (2012) 757–771.

[14] A. Young, J. Farman, R. Miller, Load alleviation technology for extending life in tidal turbines, in: Progress in Renewable Energies Offshore-Proceedings of 2nd International Conference on Renewable Energies Offshore, RENEW 2016, 2016, pp. 521–530.

[15] A. MacGillivray, H. Jeffrey, C. Hanmer, D. Magagna, A. Raventos, A. Badcock-Broe, Ocean Energy Technology: Gaps and Barriers, 2013. URL: www.si-ocean.eu.

[16] D. Magagna, L. Margheritini, Workshop on identification of future emerging technologies in the wind power sector, Technical Report March, Joint Research Centre, European Commission's science and knowledge service, 2018. doi:10.2760/23207.

[17] H. Schlichting, K. Gersten, Boundary-layer theory, Springer, 2016.

[18] D. R. Noble, T. Davey, H. C. Smith, P. Kaklis, A. Robinson, T. Bruce, Spatial variation in currents generated in the flowave ocean energy research facility, in: Proceedings of the 11th European Wave and Tidal Energy Conference (EWTEC2015), Nantes, France, 2015, pp. 6–11.

[19] H. . S. Executive, Environmental considerations, 2001. `http://https://www.hse.gov.uk/research/otopdf/2001/oto01010.pdf`.

[20] T. Burton, N. Jenkins, D. Sharpe, E. Bossanyi, Wind energy handbook, John Wiley & Sons, 2011.

[21] T. Theodorsen, General theory of aerodynamic instability and mechanism of flutter, 1935.

[22] G. S. Bir, M. J. Lawson, Y. Li, Structural design of a horizontal-axis tidal current turbine composite blade, ASME 2011 30th International Conference on Ocean, Offshore and Arctic Engineering (2011) 797–808.

[23] C. Lanczos, The Variational Principles of Mechanics, Dover Books On Physics, Dover Publications, 1970.

[24] A. Medina, M. Hemati, Lift disturbance cancellation with fast-flap actuation, in: 2018 Fluid Dynamics Conference, 2018, p. 3090.

[25] G. I. Gretton, D. M. Ingram, Development of a computational fluid dynamics model for a horizontal axis tidal current turbine, Tech. rep. for the PerAWAT project, The University of Edinburgh, 2011.

[26] I. Abbott, A. Von Doenhoff, Theory of Wing Sections, Including a Summary of Airfoil Data, Dover Books on Aeronautical Engineering Series, Dover Publications, 1959.

[27] W. Sheng, R. A. M. Galbraith, F. N. Coton, Applications of low-speed dynamic-stall model to the nrel airfoils, Journal of Solar Energy Engineering 132 (2010).

[28] W. Dai, G. Pisetta, I. M. Viola, Morphing blades for passive load control of tidal turbines, EWTEC proceedings (2019).

[29] X. Shen, X. Zhu, Z. Du, Wind turbine aerodynamics and loads control in wind shear flow, Energy 36 (2011) 1424 – 1434.